Atomic lattice resolved electron tomography of a 3D self-assembled mesocrystal

Xiaolei Chu,[1] Alex Abelson,[2] Caroline Qian,[3] Oleg Igouchkine,[4] Ethan Field,[1] Kwan-Liu Ma,[4] Matt Law[2,3,5] and Adam J. Moulé[6*]

[1] Department of Materials Science and Engineering, University of California - Davis, Davis, CA. 95616 USA

[2] Department of Materials Science and Engineering, University of California - Irvine, Irvine, CA. 92617 USA

[3] Department of Chemical and Biomolecular Engineering, University of California - Irvine, Irvine, CA. 92617 USA

[4] Department of Applied Math, University of California – Davis, Davis, CA. 95616 USA

[5] Department of Chemistry, University of California - Irvine, Irvine, CA. 92617 USA

[6]Department of Chemical Engineering, University of California - Davis, Davis, CA. 95616 USA

[*]To whom correspondence should be addressed; E-mail: amoule@ucdavis.edu

Complex three-dimensional (3D) architectures of nanoscale building blocks can be created by self-assembly, but characterizing the atomic to nanoscale structure of such materials is limited by the difficulty of visualizing atoms across mesoscopic length scales. Here we demonstrate the use of scanning transmission electron microscopy (STEM) and full-tilt tomographic reconstruction to resolve a single crystal 3D superlattice of 633 colloidal PbSe quantum dots (QDs) with a real-space resolution of 2.16 Å. The combined real-space and reciprocal-space analysis enables 3D mesoscale correlations of superlattice and atomic lattice across hundreds of crystalline domains for the first time. Inhomogeneity in position

and orientation order reveal how surface layers template the superlattice order and how the fabrication process increases orientational entropy more in interior QD layers compared to surface layers. The measurement and analysis techniques presented here have applications to a broad range of 3D nanostructured materials.

Introduction

Nanostructured materials with ordering across multiple length scales are increasingly studied for application in catalysis (zeolites[1,2] and metal-organic frameworks[3]), hydrogen production[4] and storage[2], emerging photovoltaics,[5-7] electricity storage (batteries[8] and supercapacitors[9]), and structural metals.[10,11] However, nanostructured materials are difficult to characterize because their macroscopic properties arise from hierarchical structures that span considerable length scales (0.01-1000 nm). Recent advances in atom probe tomography[12-14], X-ray ptychography[15,16], and electron tomography (ET)[17-20] have increasingly enabled structural and chemical mapping of nanomaterials over mesoscopic length scales. All-atom counting techniques have been used to identify every atom in single-crystalline and polycrystalline nanoparticles[21,22] as well as nanoparticle monolayers.[23] 4D scanning transmission electron microscopy (STEM) combines real-space and convergent beam electron diffraction imaging, but does not enable resolution of depth information.[23-26] Here we present the first demonstration of nanoparticle-by-nanoparticle orientation analysis from lattice-resolved ET, which combines real-space and reciprocal-space imaging resolved in all three spatial dimensions, using a self-assembled 3D epitaxially-fused superlattice (epi-SL) of PbSe QDs as a test sample. Using a tomogram with a spatial resolution of 2.16 Å, we determine the orientation and local lattice parameters of the superlattice (SL), the orientation of the atomic lattice (AL) of each QD, and the number, size and shape of the epitaxial

connections (necks) between the QDs. The clear breakthrough is the new ability to map position/orientation anisotropy from atomic- to meso-scale, which is critical knowledge for characterization of 3D nanostructured materials.

To demonstrate atomic lattice resolved electron tomography on the mesoscale, we acquired and analyzed a full-tilt ET dataset for a multilayer (3D) PbSe QDs epi-SL. Epi-SLs are crystals of colloidal QDs with exceptionally high spatial order. The high spatial order and ordered epitaxial necks between nearest neighbor QDs provide for strong inter-QD electronic coupling, making epi-SLs promising materials for exhibiting delocalized electronic mini-bands and serving as a versatile class of QD solids for next-generation optoelectronics.[27-32] However, current epi-SLs contain significant concentrations of structural defects (variations in QD position and orientation, the number, size and shape of necks, and QD size and shape) that localize carriers and prevent coherent electronic transport. Rational improvements to synthesis/fabrication of more perfect 3D epi-SLs is contingent upon acquisition of structural information from characterization methods that are capable of mapping defects throughout the volume of an epi-SL and down to the atomic scale, a challenging task. Conventional (S)TEM imaging and diffraction methods cannot provide internal structural details of 3D samples.[27,28,33,34] ET, in which a 3D object is reconstructed from a series of 2D images taken at a series of tilt angles, has been used to establish the basic unit cell of non-fused unary, binary, and ternary QD SLs[35-37] as well as 2D honeycomb epi-SLs[38] and thin multilayer honeycomb epi-SLs,[39] but none of these tomograms approached atomic resolution. We recently reported an electron tomogram of a polycrystalline 3D epi-SL with a resolution of 6.5 Å, sufficient to see the location, size and shape of all 1,846 PbSe QDs and their necks, but not the atomic lattice.[40] By leveraging improvements in 2D STEM resolution, use of a full-tilt sample holder, reduced FIB needle sample volume, improved reconstruction alignment, and a graphics

processing unit (GPU) based computer that was optimized for image reconstruction, we show that it is now possible to produce tomograms of sufficient resolution (2.16 Å) to image the atomic lattice of every QD in a 3D epi-SL and to provide a detailed and accurate map of both the atomic lattice and the superlattice. The unprecedented structural detail of atomic lattice resolved mesoscale ET will enable new insights into processing-structure-property relationships for QD epi-SLs and other nanostructured and mesoscale materials.

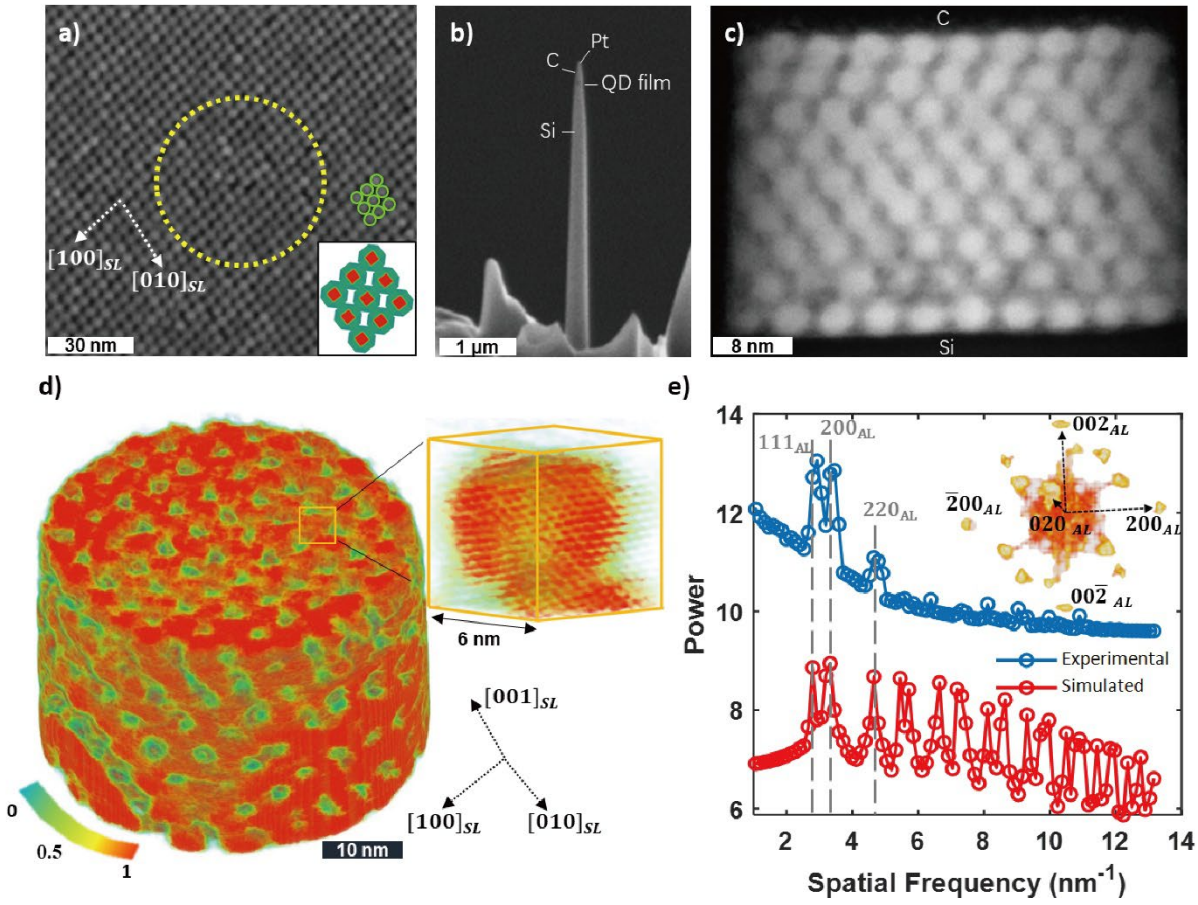

Fig. 1. Lattice-resolved electron tomogram of a PbSe QD epi-SL grain: *a) SEM image of a (100)$_{SL}$-oriented epi-SL grain. The dashed circle denotes the part of the sample that was extracted for electron tomography analysis, the inset images show a model of the surface superlattice structure, with color to highlight the facets of the quantum dots. The white arrows denote the directions of the superlattice vectors [001]$_{SL}$ and [010]$_{SL}$. b) SEM image of the FIB-prepared tomography needle. The epi-SL is located near the tip of the silicon needle capped with carbon and platinum from FIB sample preparation. c) A single HAADF-STEM image of the epi-SL disc (~60 nm diameter × ~40 nm thick). d) Perspective view of the entire tomogram and a magnified view of a single QD demonstrating 3D lattice resolution with the {220}c lattice fringes clearly visible. The color scale represents normalized intensity value of the tomogram. The dashed arrows provide visual guidance for the three SL directions e) 1D power spectrum of the 3D Fourier transform of the tomogram (blue) compared to a simulated FFT of the Pb lattice in PbSe (red). The simulated FFT is broadened from the point spread function and represents the upper limit of tomographic resolution considering both thermal and instrumental factors. The vertical dashed lines denote the {111}$_{AL}$, {200}$_{AL}$ and {220}$_{AL}$ planes, corresponding to d-spacings of 3.52 Å, 3.05 Å and 2.16 Å, respectively. Inset is the 3D power spectrum of the tomogram with all 200 Bragg spots denoted.*

MAPPING QD POSITIONS AND ORIENTATIONS

Several ET 3D reconstructions were created from a series of 2D high-angle annular dark field (HAADF) STEM images taken at different tilt angles. The multilayer (3D) QD epi-SL, fabricated as previously described,[40,41] was milled into several needles to enable acquisition of images over a full 180° angular range to help avoid reconstruction artifacts.[42] Figs. 1a and 1b show SEM images of the epi-SL film on a silicon substrate and the sample #1 tomography needle extracted from the film by focused ion beam (FIB) milling,[43] respectively. Fig. 1c shows one of the 2D STEM projections. The highest resolution 3D tomographic reconstruction was obtained from a 60 nm wide × 40 nm tall disc-shaped epi-SL sample is presented in Fig. 1d. Further sample preparation and tomographic reconstruction details can be found in Section 1 of the Supplementary Information (SI) and a full tilt-series of 2D images and the completed reconstruction are separate movie files in the SI. Projections and results from a separate tomographic reconstruction from the same film but with lower resolution are also presented in the SI. The center-of-mass (CoM) positions of all 633 QDs in the sample, described by the matrix $P_i^{SL} = [x_i, y_i, z_i]$, where i is the QD index, were determined by iteratively convoluting the tomogram with a digital mask of a QD extracted from the original tomogram volume as described in Section 2 of the SI. The SL structure is defined by unit vectors connecting the CoM positions of nearest-neighbor (NN) QDs as described by the matrix $R_i^{SL} = [\vec{A}_i, \vec{B}_i, \vec{C}_i]$, where $\vec{A}_i = [100]_{\mathrm{SL}}$, $\vec{B}_i = [010]_{\mathrm{SL}}$ and $\vec{C}_i = [001]_{\mathrm{SL}}$.

The inset of Fig. 1d shows an intensity pattern depicting the location of the Pb atoms. While the lattice fringes of PbSe are clearly visible throughout the volume of the tomogram, it was not possible to resolve every Pb atom in the sample or consistently detect the lighter Se atoms in the background of heavier Pb atoms within this large volume. Instead, we performed a windowed

Fourier analysis of the volume around each QD CoM to determine the AL spacing and orientation of each QD in the sample as described in Section 3 of the SI. The inset of Fig. 1e shows the 3D FFT of the entire volume with the $\{200\}_{AL}$ Bragg spots annotated. Fig. 1e (blue) shows the 1D power spectrum along with the simulated reference for rock salt PbSe (red). The experimental spectrum shows peaks at spatial frequencies corresponding to PbSe d_{111} = 3.52 Å, d_{200} = 3.05 Å, and d_{220} = 2.16 Å. The spatial resolution of the tomogram is determined to be 1.85-2.16 Å using the visible d_{200} and missing d_{311} diffraction peaks. We converted the Bragg spots in reciprocal space into a set of three mutually-orthonormal AL basis vectors ($R_i^{AL} = [\vec{a}, \vec{b}, \vec{c}]_i$) that describe the 3D orientation of each QD with an angular uncertainty of 1.9°. Together, P^{SL}, R^{AL}, and R^{SL} provide measurements of position, AL orientation, and relative SL orientation for each QD, respectively.

MULTI-DIMENSIONAL DATA VISUALIZATION

We used a glyph-stick representation to better represent the position, orientation, and their variance across the epi-SL (Fig. 2a-c). In this representation, each cuboid glyph represents a QD centered at P_i^{SL} and oriented at R_i^{AL}, with the cuboid faces representing the $(100)_{AL}$ planes. The glyph color represents the average orientational misalignment (defined below and in Sections 5 and 7 of the SI). We measured the thickness of each epitaxial neck between the QDs and represent the presence of a neck with a stick along the local SL vector connecting QD CoMs. The relative thickness of the neck is represented using the stick color. Figs. 2b and 2c show an overlay of tomogram slices and glyph-stick representations for SL layers C1 and C5 (C denotes the plane normal SL lattice direction, C1 is the bottom plane, C9 is the top plane). This comparison underscores the necessity to represent this highly-complex sample using a visualization that highlights spatial correlations that cannot be directly interpreted by inspection of the tomogram

itself. The complete set of raw tomogram slices and corresponding glyph-stick visualizations along all SL lattice directions are provided in Section 4 of the SI.

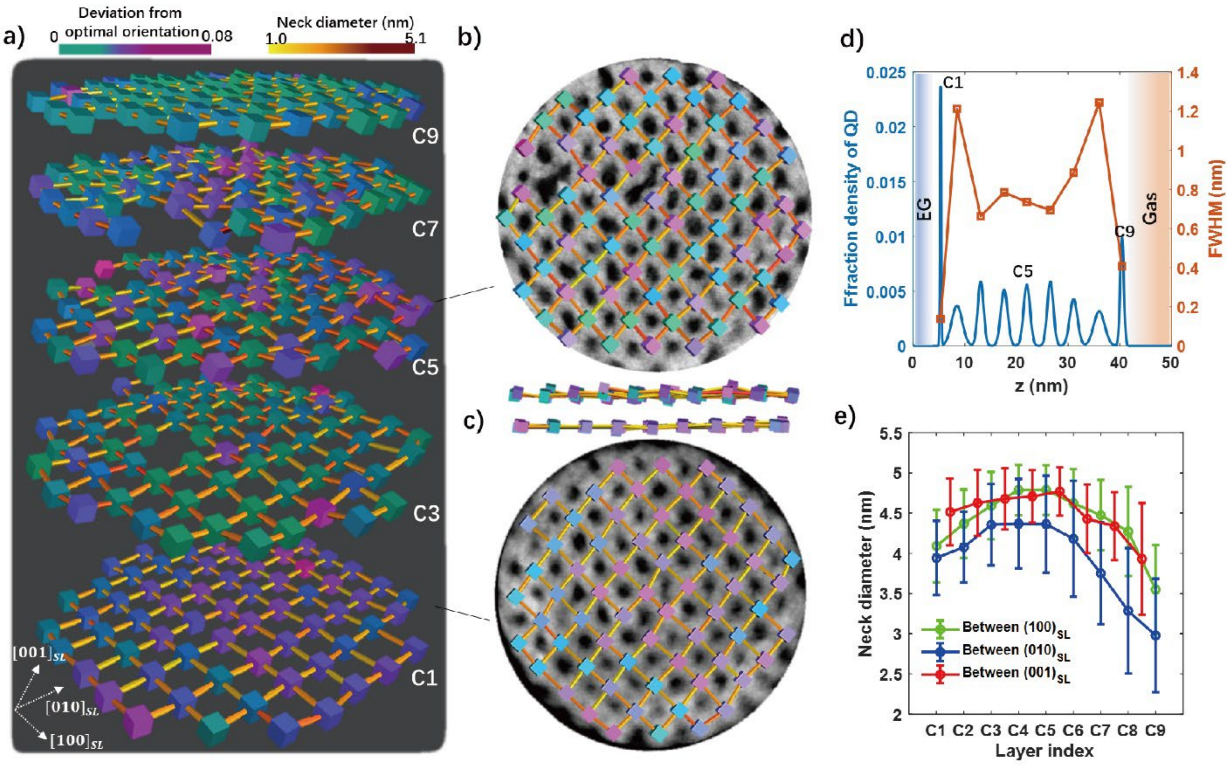

Fig. 2. Tomographic visualization of the epi-SL: *a) Exploded cube-stick view of every odd $(100)_{SL}$ layer of the sample (C1, C3, C5, C7, and C9). C1 is the bottom layer of the film (formed at the interface with ethylene glychol) and C9 is the top layer of the film (formed at the gas interface). Glyph positions and orientations denote QD positions and orientations, while the sticks represent the necks between QDs. The glyph color indicates QD misorientation relative to R_{AL}^{mono} and the stick color indicates neck diameter. (b-c) Plan and side views of C1 and C5. Each plan view shows a tomographic slice overlaid with the glyph-stack model. (d) Plot of the distribution of the vertical component of each QD position (blue, left axis) and its FWHM (orange, right axis) for C1-C9. The orange line is a guide to the eye. (e) Plot of the average inter-QD neck diameter between $(100)_{SL}$ (green), $(010)_{SL}$ (blue) and $(001)_{SL}$ (red) planes. Error bars represent one standard deviation.*

This epi-SL sample is composed of a single triclinic SL grain with no grain boundaries. The QDs assemble into nine in-plane layers with the $(100)_{SL}$ plane oriented parallel to the substrate. This sample is more uniform than previously reported 3D PbSe epi-SL samples, which is demonstrated by fewer SL point vacancies or interstitial QDs (2.2% vs 10%), improved QD connectivity (89.3% compared to 75%), and a narrower distribution of neck diameters (±0.9 nm compared to ±1.5 nm).[40] A quantitative comparison of all SL unit cell parameters is in Table S2 of the SI.

The lattice-resolved tomogram is a high-resolution map of QD positions, orientations and necks that can be used to quantify the spatial variability of structural order within the epi-SL. We use components of $R_i^{SL} = [\vec{A}_i, \vec{B}_i, \vec{C}_i]$ averaged over all QDs in a layer, where C1 is the first layer of the $[001]_{SL}$. The map shows that the top and bottom QD monolayers of the sample (C1 and C9) are strikingly more perfect than the interior layers (C2-C8). Fig. 2a-c illustrates that C1 and C9 are more planar, QDs have less orientational disorder, no point defects, and higher connectivity. Layer planarity was measured by fitting the width of the distribution (FWHM) of the vertical component of each QD position (P^{SL}) versus the layer index (Fig. 2e). We found much smaller FWHM values for C1 and C9 (0.1-0.4 nm) than C2 and C8 (~1.2 nm) and C3-C7 (0.7-1.0 nm). In contrast, the A and B layers had similar planarity throughout the sample (Fig. S12). The large and unique difference in planarity, orientation order, and reduced point defects between the surface layers and interior layers indicates that QDs at the liquid/film and film/gas interfaces experience significant ordering due to ligand/fluid interactions during self-assembly and epi-fusion compared to the QDs in the middle layers of the film. This means specifically that 2D epi-SL samples and surface specific measurement of 3D epi-SLs make poor models for multi-layer QD epi-SLs. Interface layer formation may play a strong role in templating inner layers. Analysis

of additional 3D epi-SLs will be needed to determine if this result is general and how to utilize the surface layer templating for fabrication of more ordered epi-SLs over larger domain areas.

Analysis of the neck thicknesses and R^{AL} do not show simple surface/bulk trends. Fig. 2e shows the diameters of the necks along all three SL directions. Generally, the neck thickness is, within error, uniform for C1-C6 and then decreases towards the top layer. We expect that a vertical gradient in neck thickness would occur as a result of ligand exchange diffusion from the liquid/liquid interface that would result in thinner necks closer to the top surface of the epi-SL. However, this trend is not clear and may become more relevant for thicker epi-SLs. A careful analysis of Fig. 2a reveals systematic and complex changes in R^{AL} as a function of the vertical layer index. C1 and C9 show less variation in AL and SL orientation (i.e., less variance in orientation and color of the cubes within a layer), which is correlated with the higher planarity of these layers. In summary, these observations demonstrate the need for 3D atomistic measurements of QD SLs, that, unlike 2D techniques (SEM, 4D STEM, AFM, STM, etc.), can reveal differences between the structure of surface vs interior layers.

In the following sections, we analyze the AL and SL orientations of the QDs as a function of their position in the epi-SL for the purpose of understanding how the epi-SL forms during ligand exchange. We know from previous work that the QDs self-assemble into a superlattice in which the atomic lattices of the QDs are aligned because of the attractive/repulsive forces between oleic acid ligands on the QD facets.[41,44,45] A ligand exchange reaction is used to remove the oleic acid (OA) ligands and leads to a coordinated formation of the triclinic epi-SL measured here. Below, we use mathematical analysis via P^{SL} R^{AL} and R^{AL} to understand the formation mechanism of epi-SL structure from the self-assembled SL.

QD ORIENTATION ANALYSIS (MESOSCALE)

In this section, we analyze the orientation distribution of the whole sample using statistical methods in order to derive trends that drive the epi-SL formation across length scales much larger than single QDs. Fig. 3a presents stereographic projections of R^{AL} (dark symbols) and R^{SL} (light symbols) for all 633 QDs. Since the AL is cubic, the lattice vectors of the AL are orthogonal. The QDs show excellent orientation uniformity with in-plane and out-of-plane angular spreads of ~3.7º and ~11.3º, respectively. The insets further breakdown the average R^{AL} as a function of in-plane layers C1-C9, which in the $[001]_{SL}$ changes systematically along the film normal (large diamonds in Fig. 3a) but not in-plane. This result shows that the R^{AL} tilts systematically out-of-plane from C1-C6 and back into alignment with the substrate plane from C7-C9. Each layers' alignment is more uniform than the global average of the full epi-SL. The QDs are most closely aligned to the film normal in layers C1 and C9, suggesting that they are strongly oriented during self-assembly at the liquid/film and film/air interfaces. The AL orientation changes 8.4° out-of-plane from C2 to C6 and then rotates back toward the film normal from C7 to C9 while also rotating within the plane of the film by several degrees. The R^{SL} vectors constitute a triclinic lattice. Therefore, the AL and SL vectors are necessarily non-collinear (as seen in Fig. 3a and Table S2). The R^{SL} show a larger angular spread than the R^{AL} with orientation spread of 9.4° in-plane and 14.2° out-of-plane. This is an interesting result because it shows that the AL orientations of the QDs are more uniform than would be expected from the SL position and orientation of the CoMs.

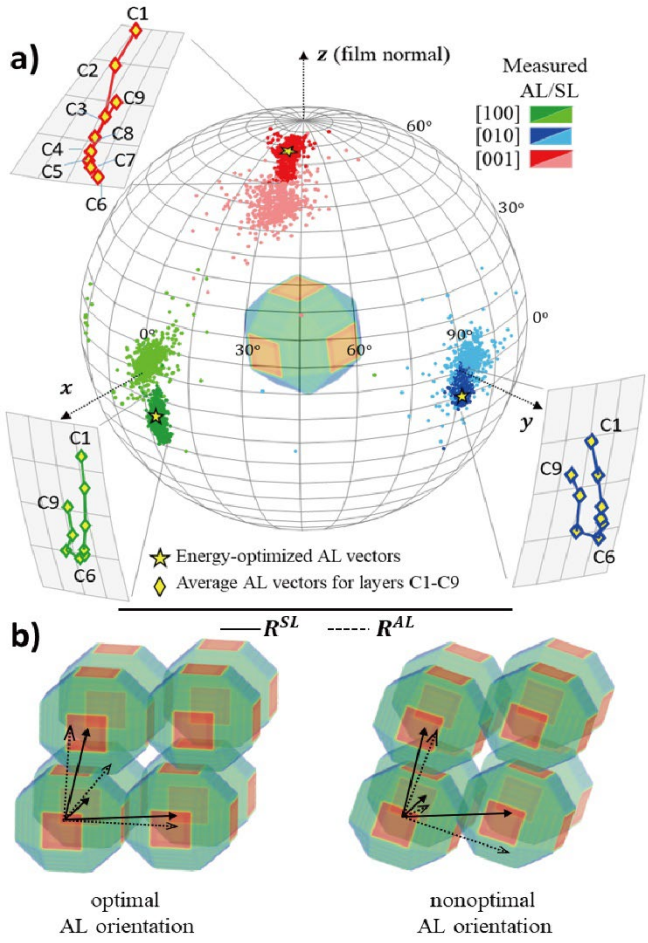

Fig. 3. Global map of QD orientations: *a) Stereographic projection of the AL and SL lattice vectors of all 633 QDs in the sample relative to the film normal: $[100]_{AL}$ (green), $[010]_{AL}$ (blue), $[001]_{AL}$ (red), $[100]_{SL}$ (lt green), $[010]_{SL}$ (lt blue) and $[001]_{SL}$ (lt red). Stars denote the calculated energy-optimized AL orientation (R^{AL}_{mono}) for the experimentally-determined SL unit cell. Diamonds are the average AL vectors for each $(001)_{SL}$ layer (C1-C9). A model of a faceted QD is inset at the center of the projection with its orientation aligned with R^{AL}_{mono}. b) Comparison of the energy-optimized epi-SL unit cell (more like surface layers) with a non-optimal unit cell (more like internal layers). Solid and dashed lines represent the lattice vectors of the SL and AL, respectively. The SL lattice vectors of the unit cells are identical.*

It is not known whether the epi-SL structure is determined thermodynamically, by minimization of the free energy, or whether the structure is kinetically trapped before complete relaxation. An energy minimized single porous crystal epi-SL structure would maximize the area overlap of the $\{100\}_{AL}$ facets between QDs and would eliminate atomic point defects and twist/tilt defects

between NN QDs. Section 5 of the SI derives an expression for the minimized single crystal global structure (R_{mono}^{AL}) as a function of the AL/SL mismatch and Table S3 shows how the unit cell changes with increasing mismatch between a cubic AL and triclinic SL. The R_{mono}^{AL} for this epi-SL is depicted as a star in Fig. 3a and the magnitude of the difference between $R_{mono}^{AL}$and the measured R^{AL} is represented by the glyph color in Fig. 2. The R_{mono}^{AL} is almost identical to the average of the R_i^{AL}, which means that R_{mono}^{AL} is a good representation of the average SL structure.

The systematic changes in R^{AL} from C1 to C9 suggest that there is no single lowest-energy AL/SL structure, but rather that different local R^{AL} are present due to differing forces in the surface and interior layers. Fig. 3b shows an optimal alignment that maximizes the co-facial overlap with QD orientation nearly aligned to the substrate plane as seen in layers C1 and C9. Towards the interior layers, the average orientation misaligns into the non-optimal structure depicted in Fig. 3b. To account for these changes in orientation, we also calculate a different energy minimized structure $\{\hat{R}_i^{AL}\}$ in which the CoMs are fixed at the measured P^{SL} and R^{SL} but the R^{AL} of each QD is oriented to maximize the overlap of the {100} facets of the QDs. We then compare the mono-crystalline and multi-crystalline orientation optimizations to the measured R^{AL} using a Pearson correlation matrix and find a better correlation to R_{mono}^{AL} than $\{\hat{R}_i^{AL}\}$. This means that the epi-SL is energetically driven towards R_{mono}^{AL} and relatively insensitive to local SL randomness. The R^{AL} distribution is narrower than the R^{SL} distribution because the R^{AL} depends more on macroscopic forces than NN positions. This effect is demonstrated by the observation that QDs adjacent to a SL vacancy are not more randomly oriented than QDs with six nearest neighbors.

The AL orientation of each QD is driven towards an energetic minimum by reaching a QD position specific balance between three factors: 1) maximizing the co-facial area of all $\{100\}_{AL}$ facets, 2) locally minimizing the nearest-neighbor AL misalignment, and 3)

the surface layer orientations are fixed by the fluid/ligand interfaces during ligand exchange while interior layers reorient to an energy minimized structure. Thus, there are differing forces on surface and bulk QD layers that result in different structures. The next section examines the NN misorientation, which focuses on understanding the energetic driver for interior layer misalignment.

QD ORIENTATION ANALYSIS (NANOSCALE)

A nanoscale approach to analyzing the AL/SL orientation begins by examining orientation at the NN level only. For every pair of NN QDs, we define a NN misorientation vector $\vec{\delta}_{ij}$ as the product of a misorientation axis $\vec{\xi}_{ij}$ and a misorientation magnitude θ_{ij} (Fig. 4a). In a perfect SL (as calculated in SI Section 5), $\vec{\delta}_{ij}$ are all zero, whereas in a randomly-oriented SL, an ensemble of $\vec{\delta}_{ij}$ occupies random points in a sphere. For the sample measured here, $\vec{\delta}_{ij}$ shows a distinct linear profile (Fig. 4b), indicating the presence of a characteristic QD rotational axis $< \vec{\xi}_{ij} >$ along $[\bar{1}20]_{AL}$. Principal component analysis (SI Section 7) shows that this rotation axis explains 89% of the variance in the NN QD misorientations, meaning that the result is statistically significant and implies that nearly all of the QDs experienced the same systematic rotation. Abelson *et al*. previously reported that the QDs rotate around a common $[110]_{AL}$ axis during ligand exchange and epitaxial fusion.[27] The difference in rotation axis ($[\bar{1}20]_{AL}$ vs. $[110]_{AL}$) between this study and that of Abelson may be associated with the more distorted triclinic SL structure of this sample. More measurements are needed to verify this hypothesis.

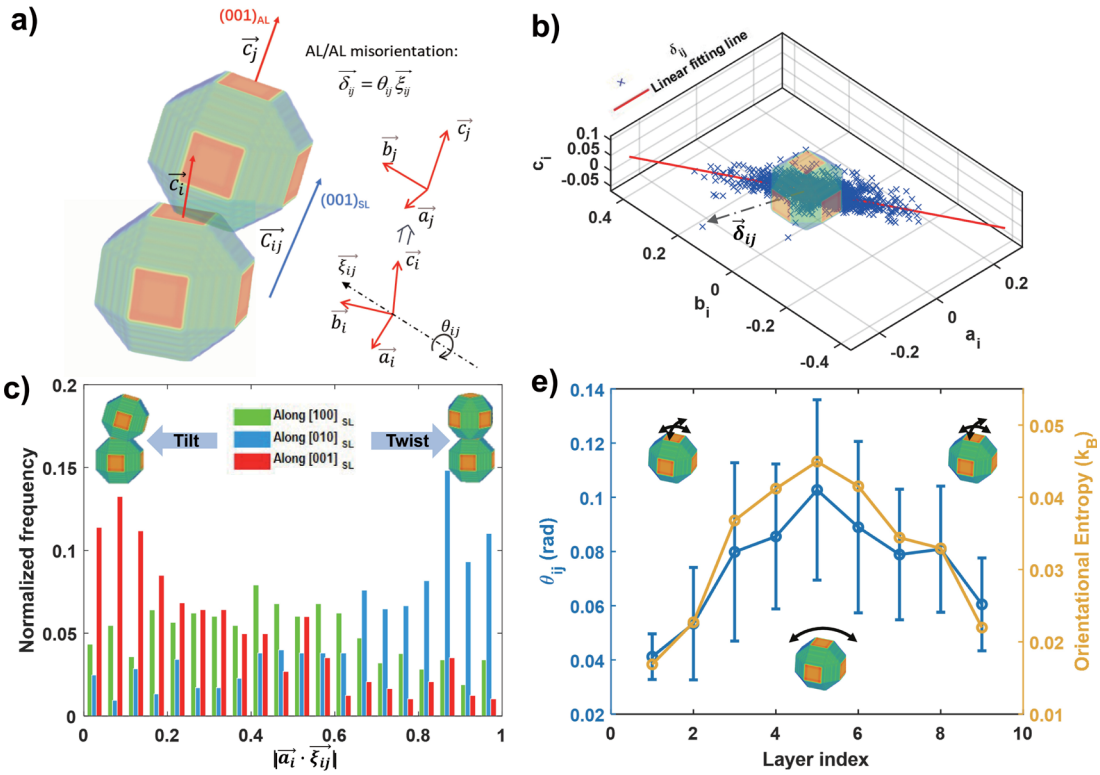

Fig. 4. Nearest neighbor orientation disorder: *a) Schematic showing the AL misorientation between nearest neighbor QDs.* $\vec{a}_i$, $\vec{b}_i$, *and* $\vec{c}_i$ *denote* $[100]_{AL}$, $[010]_{AL}$ *and* $[001]_{AL}$ *respectively. b) Scatter plot and linear regression fit of* $\vec{\delta}_{ij}$ *(NN misorientation vector) expressed in terms of the components* $\vec{a}_i$, $\vec{b}_i$, *and* $\vec{c}_i$. *A QD is inset in the center of this panel for reference. c) Histograms of* $|\vec{a}_i \cdot \vec{\xi}_{ij}|$ *(cosine between the reorientation axis and the AL vector pertinent to the co-facet) showing distinct tilt/twist misorientation character along the different SL directions. Along* $[100]_{AL}$ *shows mixed tilt/twist,* $[010]_{AL}$ *shows primarily twist, and* $[001]_{AL}$ *shows primarily tilt misorientations. d) Depicts the NN misorientation magnitude* θ_{ij} *(blue) and orientational entropy (orange) as a function of the vertical layer index.*

A direct result of the characteristic reorientation axis is that the triclinic SL shows different ratios of tilt versus twist NN misorientation components along different SL vectors. The dot product $|\vec{a}_i \cdot \vec{\xi}_{ij}|$ is a measure of the degree of tilt vs. twist misorientation of each QD pair, with a value of zero indicating pure tilt and one indicating pure twist.[23,46,47] Fig. 4c shows a histogram of $|\vec{a}_i \cdot \vec{\xi}_{ij}|$ for every interface between the 633 QDs normalized for each of the three SL directions. In the out-of-plane direction ($[001]_{SL}$) there are more tilt misorientations (average dot product of

0.23), as would be expected from the analysis in Fig. 3a. In-plane, Fig. 4c shows a high degree of twist misorientation along $[010]_{SL}$ (average dot product of 0.78) but a nearly equal mixture of tilt/twist along $[100]_{SL}$ (average dot product of 0.44). The in-plane anisotropy of twist/tilt misorientation is further evidence that the QDs experienced a collective roll in the same direction during the ligand exchange process.

One remaining mystery from the tomographic data is to understand how layer index and orientation disorder are correlated. Fig. 2d shows that C1 and C9 are most planar (have lowest position disorder) while C2 and C8 have the highest position disorder. In contrast, the R^{AL} changes gradually to the center layers and does not show an abrupt change between the surface and interior layers. The layer dependent orientation disorder can be quantified by examining the misorientation magnitude (θ_{ij}) as a function of the layer index (Fig. 4d), which shows considerably higher average orientation misalignment in the interior layers, consistent with the mesoscale analysis of QD orientation. But a higher average NN misorientation magnitude (θ_{ij}) is not the same as a broader distribution of alignments. A more direct measure of orientation distribution is orientation entropy, which quantifies the randomness of the orientation distribution in 3D space for each layer (SI Section 8).[48-50] Fig. 4d shows that the orientational entropy and θ_{ij} follow the same trend. Both the average NN misalignment and the distribution of NN misalignments increase from C1 to C5 and decrease from C5 to C9. This last result shows that the position and orientation of the C1 and C9 interface layers remain more fixed during ligand exchange while the QDs in interior layers are more free to misorient. The volume reduction during ligand exchange results in a collective roll of the QDs along the $[\bar{1}20]_{AL}$ direction that is more pronounced in interior layers. The contrast between surface and interior layers also results in greater random misalignment (higher entropy) in the interior layers.

KINETICALLY TRAPPED STRUCTURE

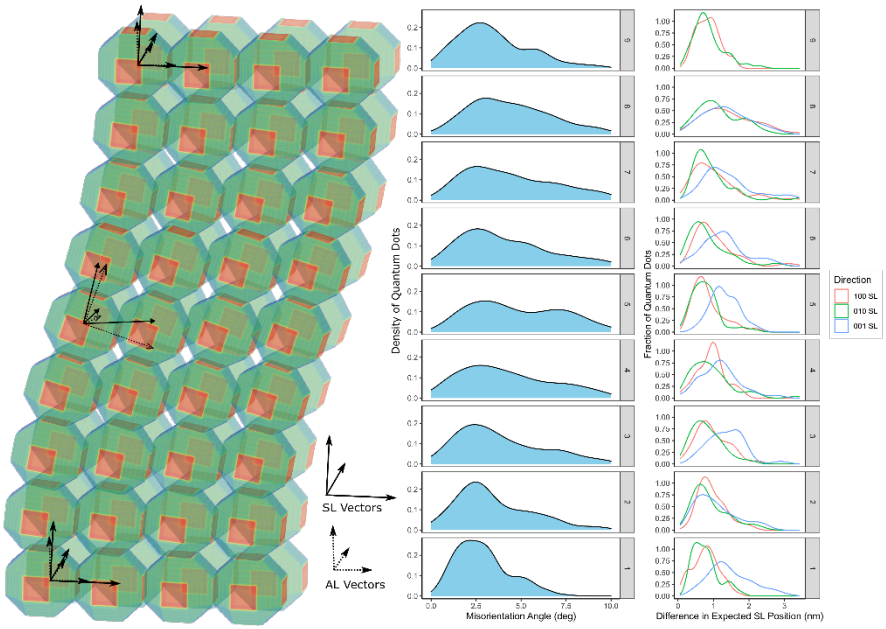

Fig. 5. Kinetically trapped SL: *a) Schematic showing the average AL and SL orientation for the multilayer film. A perfect triclinic SL (see SI Tab. S3) has perfectly aligned AL interfaces. b) The distribution QD misorientation with respect to a fully aligned lattice as a function of layer index. c) The distribution of CoM positions (along $(100)_{SL}$, $(010)_{SL}$, and $(001)_{SL}$) with respect to a fully aligned lattice as a function of layer index. A perfectly positioned and aligned QD would have a value of zero in both distributions.*

In Table S3 of the SI, we show images of the energy minimized epi-SL structures as a function of the triclinic angles. For every structure, the electronic disorder for the epi-SL is minimized by reduction of position disorder, SL orientation disorder, and AL orientation disorder. Fig. 5a shows a schematic cartoon of the 9-layer stack showing the systematic change in Al orientation, a change that requires tomographic measurement to capture. The fact that not all AL vectors are aligned and that center layers have different orientation shows that the epi-SL structure is kinetically trapped. There is an enthalpic driving force towards removal of high energy atomic dislocations between QDs, but the tilt and twist defects show that the epi-SL was frozen via NN neck formation before these defects could be resolved.[23,47,51-54] The clear collective orientation

behavior shows that the ligand exchange is a collective topo-epitaxy[41] and not by formation of NN attachements.[55] Figs. 5b and 5c show the orientation and position differences (respectively) between the fully relaxed SL and the measured SL. Fig. 5b shows that the QDs are on average misaligned by 2.5° but with a larger range of misalignment angles for center SL layers compared to surface layers. This is a second measurement of increased orientational entropy for center layers. Fig. 5c shows the distance between the expected relaxed and actual QD location. Consistent with prior measurements, the top and bottom layers have a narrower distribution of differences compared to center layers. The largest position deviation even within each layer is along the $[001]_{SL}$ direction, which is the same axis for the orientational anisotropy. Thus all of the measurements point to a collective orientation change through the layers that is correlated with a specific rotation axis and increased position and orientation anisotropy in center layers.

Conclusions

We used high-resolution and large-volume lattice resolved electron tomography combined with Fourier analysis to generate the first 3D lattice resolved tomographic image of a PbSe - epitaxially fused quantum dot superlattice. We resolved 633 QDs with 2.16 Å resolution allowing for quantitative determination of QD position, orientation and connectivity in three dimensions. Lattice resolved tomography enables mapping of the orientations of the nanocrystalline building blocks of 3D mesomaterials, which was unfeasible until now. This new measurement capability will be enabling for emerging nanostructured metals, energy storage, photovoltaic, gas storage, and catalysis materials.

A detailed analysis of the correlations between QD position, superlattice orientation, and atomic lattice orientation are diagnostic for the formation mechanism of the epitaxial QD

superlattice. We show that the interface layers have much higher positional order, fewer superlattice point defects, higher nearest neighbor neck connectivity, and lower orientational anisotropy than interior layers. The QDs in the interface layer are more oriented towards each other within the substrate plane and maximize the co-facial overlap between nearest neighbors. This result shows that measurements of epi-SLs, that acquire either surface information or average bulk information, will generate a misleading and incomplete understanding of 3D nanostructured materials. Towards the interior layers, the average atomic lattice orientation rotates systematically out-of-plane resulting in a tilted epi-SL that none-the-less maximizes the interfacial overlap, which shows that the local AL orientation order is energetically determined. Analysis of the nearest neighbor misalignment demonstrates a common in-plane rotation axis for QDs that occurs during the ligand exchange process. The average nearest neighbor misalignment, deviation of misalignments, and orientational entropy all increase towards center layers. These results have huge implications for fabrication of thicker and more perfect epi-SL samples. The high order of surface layers is a strength, but mismatch between the cubic AL and triclinic SL necessitates relaxation of the positions and orientations of interior QDs. The ligand exchange process causes a systematic "roll" of QDs in one direction that is more pronounced in interior layers.

This work informs changes to the processing of epi-SL samples to reduce disorder and increase delocalization of mini-band states. Here we demonstrated that the mismatch between the cubic AL lattice and triclinic SL lattice reduces the nearest neighbor epitaxial overlap of the (001) facets on QDs. A logical method to improve epi-SL order should focus on controlling the ligand exchange kinetics to achieve a more cubic SL and reduce orientational entropy in interior layers. For the $(001)_{SL}$ oriented epi-SL shown here, the highly ordered and aligned surface layers counterintuitively causes increased misalignment in interior layers during the ligand exchange.

References

1 Davis, M. E. Ordered porous materials for emerging applications. *Nature* **417**, 813-821, doi:10.1038/nature00785 (2002).

2 Arico, A. S., Bruce, P., Scrosati, B., Tarascon, J. M. & Van Schalkwijk, W. Nanostructured materials for advanced energy conversion and storage devices. *Nature Materials* **4**, 366-377, doi:10.1038/nmat1368 (2005).

3 Lee, J. *et al.* Metal-organic framework materials as catalysts. *Chemical Society Reviews* **38**, 1450-1459, doi:10.1039/b807080f (2009).

4 Kudo, A. & Miseki, Y. Heterogeneous photocatalyst materials for water splitting. *Chemical Society Reviews* **38**, 253-278, doi:10.1039/b800489g (2009).

5 Tsai, H. H. *et al.* High-efficiency two-dimensional Ruddlesden-Popper perovskite solar cells. *Nature* **536**, 312-+, doi:10.1038/nature18306 (2016).

6 Swarnkar, A. *et al.* Quantum dot-induced phase stabilization of alpha-CsPbI3 perovskite for high-efficiency photovoltaics. *Science* **354**, 92-95, doi:10.1126/science.aag2700 (2016).

7 Oregan, B. & Grätzel, M. A Low-Cost, High-Efficiency Solar-Cell Based on Dye-Sensitized Colloidal Tio2 Films. *Nature* **353**, 737-740 (1991).

8 Chan, C. K. *et al.* High-performance lithium battery anodes using silicon nanowires. *Nature Nanotechnology* **3**, 31-35, doi:10.1038/nnano.2007.411 (2008).

9 Wang, G. P., Zhang, L. & Zhang, J. J. A review of electrode materials for electrochemical supercapacitors. *Chemical Society Reviews* **41**, 797-828, doi:10.1039/c1cs15060j (2012).

10 Kumar, K. S., Van Swygenhoven, H. & Suresh, S. Mechanical behavior of nanocrystalline metals and alloys. *Acta Materialia* **51**, 5743-5774, doi:10.1016/j.actamat.2003.08.032 (2003).

11 Wang, Y. M., Chen, M. W., Zhou, F. H. & Ma, E. High tensile ductility in a nanostructured metal. *Nature* **419**, 912-915, doi:10.1038/nature01133 (2002).

12 Devaraj, A. *et al.* Three-dimensional nanoscale characterisation of materials by atom probe tomography. *International Materials Reviews* **63**, 68-101, doi:10.1080/09506608.2016.1270728 (2018).

13 Gross, L., Mohn, F., Moll, N., Liljeroth, P. & Meyer, G. The Chemical Structure of a Molecule Resolved by Atomic Force Microscopy. *Science* **325**, 1110-1114, doi:10.1126/science.1176210 (2009).

14 Seidman, D. N. Three-dimensional atom-probe tomography: Advances and applications. *Annual Review of Materials Research* **37**, 127-158, doi:10.1146/annurev.matsci.37.052506.084200 (2007).

15 Pfeiffer, F. X-ray ptychography. *Nature Photonics* **12**, 9-17, doi:10.1038/s41566-017-0072-5 (2018).

16 Aaron Michelson, B. M., Hamed Emamy, Xiaojing Huang, Yong S. Chu, Hanfei Yan, and Oleg Gang. Three-dimensional visualization of nanoparticlelattices and multimaterial frameworks. *Science* **376**, 203-207 (2022).

17 Song, H. *et al.* Electron Tomography: A Unique Tool Solving Intricate Hollow Nanostructures. *Advanced Materials* **31**, doi:10.1002/adma.201801564 (2019).

18 Gajjela, R. S. R. & Koenraad, P. M. Atomic-Scale Characterization of Droplet Epitaxy

Quantum Dots. *Nanomaterials* **11**, doi:10.3390/nano11010085 (2021).
19 Midgley, P. A. & Dunin-Borkowski, R. E. Electron tomography and holography in materials science. *Nature Materials* **8**, 271-280, doi:10.1038/nmat2406 (2009).
20 Han, H. X. *et al.* Multiscale hierarchical structures from a nanocluster mesophase. *Nature Materials* **21**, 518-+, doi:10.1038/s41563-022-01223-3 (2022).
21 Miao, J., Ercius, P. & Billinge, S. J. Atomic electron tomography: 3D structures without crystals. *Science* **353**, aaf2157 (2016).
22 Midgley, P. A. & Weyland, M. 3D electron microscopy in the physical sciences: the development of Z-contrast and EFTEM tomography. *Ultramicroscopy* **96**, 413-431, doi:10.1016/s0304-3991(03)00105-0 (2003).
23 Smeaton, M. A., El Baggari, I., Balazs, D. M., Hanrath, T. & Kourkoutis, L. F. Mapping Defect Relaxation in Quantum Dot Solids upon In Situ Heating. *Acs Nano* **15**, 719-726, doi:10.1021/acsnano.0c06990 (2021).
24 Ophus, C. Four-Dimensional Scanning Transmission Electron Microscopy (4D-STEM): From Scanning Nanodiffraction to Ptychography and Beyond. *Microscopy and Microanalysis* **25**, 563-582, doi:10.1017/s1431927619000497 (2019).
25 Yang, H. *et al.* in *Electron Microscopy and Analysis Group Conference (EMAG).* (2015).
26 Jarausch, K., Thomas, P., Leonard, D. N., Twesten, R. & Booth, C. R. Four-dimensional STEM-EELS: Enabling nano-scale chemical tomography. *Ultramicroscopy* **109**, 326-337, doi:10.1016/j.ultramic.2008.12.012 (2009).
27 Abelson, A. *et al.* Collective topo-epitaxy in the self-assembly of a 3D quantum dot superlattice. *Nature Materials* **19**, 49-+, doi:10.1038/s41563-019-0485-2 (2020).
28 Baumgardner, W. J., Whitham, K. & Hanrath, T. Confined-but-Connected Quantum Solids via Controlled Ligand Displacement. *Nano Letters* **13**, 3225-3231, doi:10.1021/nl401298s (2013).
29 Jiang, C. W. & Green, M. A. Silicon quantum dot superlattices: Modeling of energy bands, densities of states, and mobilities for silicon tandem solar cell applications. *Journal of Applied Physics* **99**, doi:10.1063/1.2203394 (2006).
30 Kalesaki, E., Evers, W. H., Allan, G., Vanmaekelbergh, D. & Delerue, C. Electronic structure of atomically coherent square semiconductor superlattices with dimensionality below two. *Physical Review B* **88**, doi:10.1103/PhysRevB.88.115431 (2013).
31 Sandeep, C. S. S. *et al.* Epitaxially Connected PbSe Quantum-Dot Films: Controlled Neck Formation and Optoelectronic Properties. *Acs Nano* **8**, 11499-11511, doi:10.1021/nn504679k (2014).
32 Whitham, K. *et al.* Charge transport and localization in atomically coherent quantum dot solids. *Nature Materials* **15**, 557-+, doi:10.1038/nmat4576 (2016).
33 Savitzky, B. H. *et al.* Propagation of Structural Disorder in Epitaxially Connected Quantum Dot Solids from Atomic to Micron Scale. *Nano Letters* **16**, 5714-5718, doi:10.1021/acs.nanolett.6b02382 (2016).
34 Whitham, K. & Hanrath, T. Formation of Epitaxially Connected Quantum Dot Solids: Nucleation and Coherent Phase Transition. *Journal of Physical Chemistry Letters* **8**, 2623-2628, doi:10.1021/acs.jpclett.7b00846 (2017).
35 Boneschanscher, M. P. *et al.* Electron Tomography Resolves a Novel Crystal Structure in a Binary Nanocrystal Superlattice. *Nano Letters* **13**, 1312-1316, doi:10.1021/nl400100c (2013).
36 Friedrich, H. *et al.* Quantitative Structural Analysis of Binary Nanocrystal Superlattices

by Electron Tomography. *Nano Letters* **9**, 2719-2724, doi:10.1021/nl901212m (2009).
37 Savitzky, B. H. *et al.* Three-Dimensional Arrangement and Connectivity of Lead-Chalcogenide Nanoparticle Assemblies for Next Generation Photovoltaics. *Microscopy and Microanalysis* **20**, 542-543, doi:10.1017/S1431927614004437 (2014).
38 Boneschanscher, M. P. *et al.* Long-range orientation and atomic attachment of nanocrystals in 2D honeycomb superlattices. *Science* **344**, 1377-1380, doi:10.1126/science.1252642 (2014).
39 Peters, J. L. *et al.* Mono- and Multilayer Silicene-Type Honeycomb Lattices by Oriented Attachment of PbSe Nanocrystals: Synthesis, Structural Characterization, and Analysis of the Disorder. *Chemistry of Materials* **30**, 4831-4837, doi:10.1021/acs.chemmater.8b02178 (2018).
40 Chu, X. *et al.* Structural characterization of a polycrystalline epitaxially-fused colloidal quantum dot superlattice by electron tomography. *Journal of Materials Chemistry A* **8**, 18254-18265, doi:10.1039/d0ta06704k (2020).
41 Abelson, A. *et al.* Collective topo-epitaxy in the self-assembly of a 3D quantum dot superlattice. *Nat Mater* **19**, 49-55, doi:10.1038/s41563-019-0485-2 (2020).
42 Goris, B., Roelandts, T., Batenburg, K., Mezerji, H. H. & Bals, S. Advanced reconstruction algorithms for electron tomography: from comparison to combination. *Ultramicroscopy* **127**, 40-47 (2013).
43 Wirth, R. Focused Ion Beam (FIB) combined with SEM and TEM: Advanced analytical tools for studies of chemical composition, microstructure and crystal structure in geomaterials on a nanometre scale. *Chemical Geology* **261**, 217-229, doi:10.1016/j.chemgeo.2008.05.019 (2009).
44 Baranov, A. V. *et al.* Self-Organization of Colloidal PbS Quantum Dots into Highly Ordered Superlattices. *Langmuir* **31**, 506-513, doi:10.1021/la503913z (2015).
45 Salzmann, B. B. V., van der Sluijs, M. M., Soligno, G. & Vanmaekelbergh, D. Oriented Attachment: From Natural Crystal Growth to a Materials Engineering Tool. *Accounts of Chemical Research* **54**, 787-797, doi:10.1021/acs.accounts.0c00739 (2021).
46 Walravens, W. *et al.* Setting Carriers Free: Healing Faulty Interfaces Promotes Delocalization and Transport in Nanocrystal Solids. *ACS Nano* **13**, 12774-12786, doi:10.1021/acsnano.9b04757 (2019).
47 Ondry, J. C., Hauwiller, M. R. & Alivisatos, A. P. Dynamics and Removal Pathway of Edge Dislocations in Imperfectly Attached PbTe Nanocrystal Pairs: Toward Design Rules for Oriented Attachment. *Acs Nano* **12**, 3178-3189, doi:10.1021/acsnano.8b00638 (2018).
48 Felippe, H. *et al.* The von Neumann entropy for the Pearson correlation matrix: A test of the entropic brain hypothesis. *arXiv* **arXiv:2106.05379**, doi: https://doi.org/10.48550/arXiv.2106.05379 (2021).
49 Lee, J., Yang, J., Kwon, S. G. & Hyeon, T. Nonclassical nucleation and growth of inorganic nanoparticles. *Nature Reviews Materials* **1**, doi:10.1038/natrevmats.2016.34 (2016).
50 Chua, E. Y. S. Does von Neumann Entropy Correspond to Thermodynamic Entropy? *Philosophy of Science* **88**, 145-168, doi:10.1086/710072 (2020).
51 Ondry, J. C., Frechette, L. B., Geissler, P. L. & Alivisatos, A. P. Trade-offs between Translational and Orientational Order in 2D Superlattices of Polygonal Nanocrystals with Differing Edge Count. *Nano Letters* **22**, 389-395, doi:10.1021/acs.nanolett.1c04058 (2022).

52 Ondry, J. C. & Alivisatos, A. P. Application of Dislocation Theory to Minimize Defects in Artificial Solids Built with Nanocrystal Building Blocks. *Accounts of Chemical Research* **54**, 1419-1429, doi:10.1021/acs.accounts.0c00719 (2021).
53 Lee, Y. H. *et al.* Modulating Orientational Order to Organize Polyhedral Nanoparticles into Plastic Crystals and Uniform Metacrystals. *Angewandte Chemie-International Edition* **59**, 21183-21189, doi:10.1002/anie.202009941 (2020).
54 Geuchies, J. J. *et al.* Unravelling three-dimensional adsorption geometries of PbSe nanocrystal monolayers at a liquid-air interface. *Communications Chemistry* **3**, doi:10.1038/s42004-020-0275-4 (2020).
55 Chen, I. Y. *et al.* The Role of Dimer Formation in the Nucleation of Superlattice Transformations and Its Impact on Disorder. *Acs Nano* **14**, 11431-11441, doi:10.1021/acsnano.0c03800 (2020).